Topological Phonons and Weyl Lines in Three Dimensions

Olaf Stenull, C. L. Kane, and T. C. Lubensky
Department of Physics and Astronomy, University of Pennsylvania, Philadelphia, Pennsylvania 19104, USA
(Received 1 June 2016; published 5 August 2016)

Topological mechanics and phononics have recently emerged as an exciting field of study. Here we introduce and study generalizations of the three-dimensional pyrochlore lattice that have topologically protected edge states and Weyl lines in their bulk phonon spectra, which lead to zero surface modes that flip from one edge to the opposite as a function of surface wave number.

DOI: 10.1103/PhysRevLett.117.068001

Mechanical lattices with a perfect balance between the number of degrees of freedom and the number of constraints (springs) with unit cells of appropriate internal geometry exhibit zero-frequency modes at boundaries even though they have very few if any zero modes (ZMs) in their bulk [1,2]. The topological origin of these ZMs was explained in Ref. [3], which introduced the framework for a phononic version of topological band theory that is well known in electronic contexts, including polyacetylene [4], quantum Hall systems [5,6], and topological insulators [7–12]. So far, attention has focused on one- [13] and two-dimensional (2D) [14–17] model systems, such as the generalized kagome lattice (GKL) [3]. In this paper, we establish the fundamental result that three-dimensional (3D) lattices exhibiting topological phonons can be constructed and explore their properties. With current 3D-printing technology, it is already possible to construct 3D metamaterials of almost limitless complexity. Our work provides templates for fabricating new materials with unusual elastic and phononic properties. We introduce a 3D generalized pyrochlore lattice (GPL) with deformed corner sharing tetrahedra, whose edges are occupied by central-force springs, as depicted in Fig. 1. We show that the bulk phonon spectrum of these lattices exhibit lines of topologically protected ZMs, analogous to lines of touching bands in line-node semimetals [18–21] and gyroid photonic crystals [22], that cause the number of protected surface modes to undergo discontinuous jumps as a function of surface wave number.

In 2D GKLs (see the Supplemental Material [23] for background information), there are lattices whose bulk vibrational spectrum is "fully gapped" at all wave vectors $\mathbf{q}$ except for the required acoustic ZMs at $\mathbf{q} = 0$. These lattices fall into topological classes distinguished by topological invariants characterizing their reciprocal-space band structure, and they exhibit topological zero-frequency edge modes whose number on a given surface is determined by bulk topological invariants and local lattice conformation at that surface. In GKLs, the transition between topologically distinct phases is marked by the existence of a line in the Brillouin zone (BZ) along which normal-mode frequencies vanish. This line of ZMs is a consequence of the existence of straight lines of bonds (filaments) that carry a state of self stress (SSS) in which the bonds are under tension but site forces vanish. The Maxwell-Calladine counting rule (see below) [24,25] applied with periodic boundary conditions then guarantees corresponding ZMs.

We find that 3D GPLs have a richer structure than 2D GKLs. Like GKLs, they exhibit gapless bulk modes associated with localized SSSs: Arrays of straight parallel lines of SSSs—six in the original pyrochlore lattice (PL) aligned along the tetrahedral edges—have associated planes of ZMs in reciprocal space aligned perpendicular to the array filaments, and flat planes of SSSs—four in the PL along the tetrahedral faces—have associated perpendicularly aligned lines of ZMs in reciprocal space. As in the GKL, the bulk ZMs on these planes (lines) can be lifted to nonzero frequency by distorting the lattice to remove the straight lines (flat planes) of bonds. However, unlike in the GKL, there are lines of bulk ZMs in reciprocal space that are protected by an integer topological invariant defined on a path that encircles them, and that influence the number

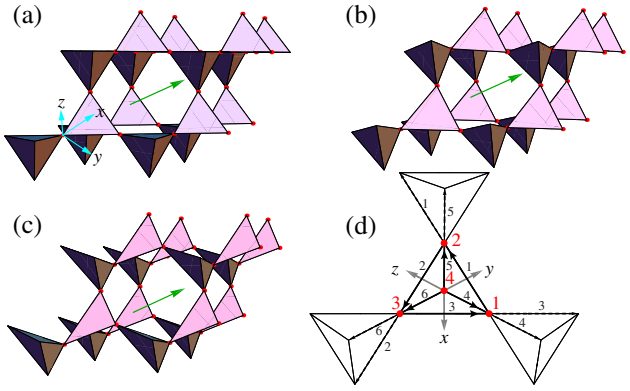

FIG. 1. The (a) PL and the GPL in the (b) X_1 and (c) X_{-1} conformations (see text). The (green) arrow represents the (1,1,1) direction. (d) The unit cell of (a) viewed along the $-\hat{\mathbf{n}}$ direction. The (red) dots with the (red) numbers mark the basis sites. The solid (dashed) arrows designate the bond vectors $\mathbf{a}_b$ ($\mathbf{a}'_b$) of the internal (external) bonds.

and location of surface ZMs. These are the mechanical analog of Weyl lines (WLs) that exist in electronic [18–21] and photonic [22] systems. Analogous Weyl-Dirac points [19,26,27] can also be present in 2D, as in the electronic spectra of graphene [28–30] and phonon spectra in deformed square lattices [16] and 2D models of jammed matter [17].

Our GPL is based on the PL with 4-site, 12-bond unit cells. Our standard reference unit cell has sites at the four corners of a tetrahedron at the basis positions $\mathbf{r}_1 = \frac{1}{2}(1,1,0)$, $\mathbf{r}_2 = \frac{1}{2}(0,1,1)$, $\mathbf{r}_3 = \frac{1}{2}(1,0,1)$, and $\mathbf{r}_4 = (0,0,0)$ and bonds as shown in Fig. 1(d). Note that this cell lacks inversion symmetry, as do all other unit cells in GPLs, and, as a result, it has a nonvanishing dipole moment when charges $+3$ are placed at its sites and charges -1 at the center of its bonds. The primitive translation vectors of the lattice are $\mathbf{T}_1 = (1,1,0)$, $\mathbf{T}_2 = (0,1,1)$, and $\mathbf{T}_3 = (1,0,1)$. There are six internal (external) bonds with bond vectors $\mathbf{a}_1$ to $\mathbf{a}_6$ ($\mathbf{a}'_1$ to $\mathbf{a}'_6$). The triangular faces of lattice tetrahedra lie in four sets of parallel planes and form kagome lattices in each. One of the four sets has its layer normal parallel to the (1,1,1) direction. In the GPL, this latter set of planes will play a distinguished role, and we will refer to it as the GKL planes.

In the PL, there are six sets of straight filaments, built from the bonds on the six edges of the tetrahedra, that carry SSSs. Following Ref. [3], our generalization is designed to convert specific straight filaments into "zigzagged" ones that do not carry SSSs. In the GPL, the positions of the basis sites are displaced relative to those of the PL, $\mathbf{r}_i \to \mathbf{r}_i + \delta\mathbf{r}_i(X)$, where

$$\delta\mathbf{r}_1(X) = x_1\sqrt{3}\hat{\mathbf{e}}_1 - x_2\hat{\mathbf{a}}_3, \tag{1a}$$

$$\delta\mathbf{r}_2(X) = x_2\sqrt{3}\hat{\mathbf{e}}_2 - x_3\hat{\mathbf{a}}_1, \tag{1b}$$

$$\delta\mathbf{r}_3(X) = x_3\sqrt{3}\hat{\mathbf{e}}_3 - x_1\hat{\mathbf{a}}_2, \tag{1c}$$

$$\delta\mathbf{r}_4(X) = -z\hat{\mathbf{n}}, \tag{1d}$$

with $X \equiv (x_1,x_2,x_3,z)$, $\hat{\mathbf{a}}_j = \mathbf{a}_j/|\mathbf{a}_j|$, $\hat{\mathbf{e}}_j = (\mathbf{a}_j \times \hat{\mathbf{n}})/|\mathbf{a}_j \times \hat{\mathbf{n}}|$, and $\hat{\mathbf{n}}$ the unit vector in the (1,1,1) direction. The parameter z determines the vertical position of site 4 relative to the GKL planes. If $z \neq 0$ and $x_1 = x_2 = x_3 = 0$, the three sets of filaments outside the GKL planes (comprised of bonds indexed by 4, 5, and 6, respectively) are zigzagged whereas the three sets of filaments within the GKL planes (comprised of bonds indexed by 1, 2, and 3, respectively) are still straight. A nonzero x_n converts the straight filament parallel to $\hat{\mathbf{a}}_n$ to a zigzag one, cf. Ref. [3]. We have also studied more general versions of our model lattice in which sites 1 to 3 can adopt positions outside the GKL planes, thereby destroying their independent SSSs. For simplicity, however, we will focus on the model lattices described by Eq. (1). More specifically, we will focus on the two lattice conformations corresponding to the parameter settings $X = X_1 \equiv (0.1, 0.1, 0.1, 0.1)$ and $X = X_{-1} \equiv (-0.1, 0.1, 0.1, 0.1)$; see Fig. 1. The GKL planes of these lattices are equivalent to the GKL conformations depicted in Figs. 2(c) and 2(e) of Ref. [3], respectively.

Any d-dimensional central force elastic network consisting of periodically repeated unit cells with n sites and n_B bonds is governed by the generalized Calladine-Maxwell theorem [1,24,25] $n_0(\mathbf{q}) - s(\mathbf{q}) = dn - n_B$ at each wave vector $\mathbf{q}$ in the BZ. It relates the number $n_0(\mathbf{q})$ of ZMs and the number $s(\mathbf{q})$ of SSSs to the invariant properties n and n_B of the unit cell and follows from the properties of the $n_B \times dn$ compatibility matrix $\mathbf{C}(\mathbf{q})$ relating bond displacements $\mathbf{u}(\mathbf{q})$ to bond extensions $\mathbf{e}(\mathbf{q})$ via $\mathbf{C}(\mathbf{q})\mathbf{u}(\mathbf{q}) = \mathbf{e}(\mathbf{q})$ and the $dn \times n_B$ equilibrium matrix $\mathbf{Q}(\mathbf{q}) = \mathbf{C}^\dagger(\mathbf{q})$ relating bond tensions $\mathbf{t}(\mathbf{q})$ to site forces $\mathbf{f}(\mathbf{q})$ via $\mathbf{Q}(\mathbf{q})\mathbf{t}(\mathbf{q}) = \mathbf{f}(\mathbf{q})$. ZMs constitute the null space of $\mathbf{C}(\mathbf{q})$ and SSSs the null space of $\mathbf{Q}(\mathbf{q})$. When all masses and spring constants are set to unity, as we have done here, the dynamical matrix governing the phonon spectrum is simply $\mathbf{D}(\mathbf{q}) = \mathbf{Q}(\mathbf{q})\mathbf{C}(\mathbf{q})$. Under periodic boundary conditions, the GPL satisfies $dn = n_B$; i.e., it is a Maxwell lattice [1] in which at each $\mathbf{q}$ including $\mathbf{q} = 0$, there is always one SSS for each ZM. The compatibility, equilibrium, and dynamical matrixes are all 12×12 matrixes (see the Supplemental Material for details [23]).

The elastic energy density can be expressed [31] in terms of the six-dimensional vector of symmetric strains $U = (u_{xx}, u_{yy}, u_{zz}, u_{xy}, u_{xz}, u_{yz})$ and the 6×6 Voigt matrix $\mathbf{K}$: $f = \frac{1}{2}U^T \cdot \mathbf{K} \cdot U$. The matrix $\mathbf{K}$ is determined by the normalized eigenvectors of the null space of $\mathbf{Q}(\mathbf{q} = 0)$ [1]. The PL has six $\mathbf{q} = 0$ SSSs, with nonzero overlap with affine strain that stabilize all six independent strains. For X_1 and X_{-1}, there are no straight filaments, but there are three $\mathbf{q} = 0$ SSSs paired with the three required $\mathbf{q} = 0$ translation ZMs. $\mathbf{K}$ has three positive and three zero eigenvalues, the latter with associated eigenvectors corresponding to three zero-energy elastic distortions of the unit cell called Guest modes [32]. For X_1, the three Guest modes are proportional to $(2,0,0,0,0,-1)$, $(0,2,0,0,-1,0)$, or $(0,0,2,-1,0,0)$. For X_{-1}, the Guest modes involve all components of $\mathbf{U}$.

The topological properties of the phononic band structure of the GPL are determined by the $\mathbf{C}$ or $\mathbf{Q}$ matrixes [3]. The determinants of these matrices map a path in $\mathbf{q}$ space onto a path in the complex plane. Because $\mathbf{Q}$ and $\mathbf{C}$ are invariant under $\mathbf{q} \to \mathbf{q} + \mathbf{G}$ for any reciprocal lattice (RL) vector $\mathbf{G}$, any path in $\mathbf{q}$ space whose start and end points are separated by a RL vector will map onto a closed path in the complex plane. For simplicity, we focus on paths in $\mathbf{q}$ space that are straight lines along the primitive vectors $\mathbf{b}_1$, $\mathbf{b}_2$, $\mathbf{b}_3$, satisfying $\mathbf{b}_i \cdot \mathbf{T}_j = 2\pi\delta_{ij}$, of the RL. The integer winding numbers of the corresponding closed paths in the complex plane are

$$m(\mathbf{q}_\perp, \mathrm{G}) = \frac{1}{2\pi i}\int_0^G dp\, \frac{d}{dp}\mathrm{LogDet}\mathbf{Q}(\mathbf{q}_\perp, p, \mathrm{G}), \tag{2}$$

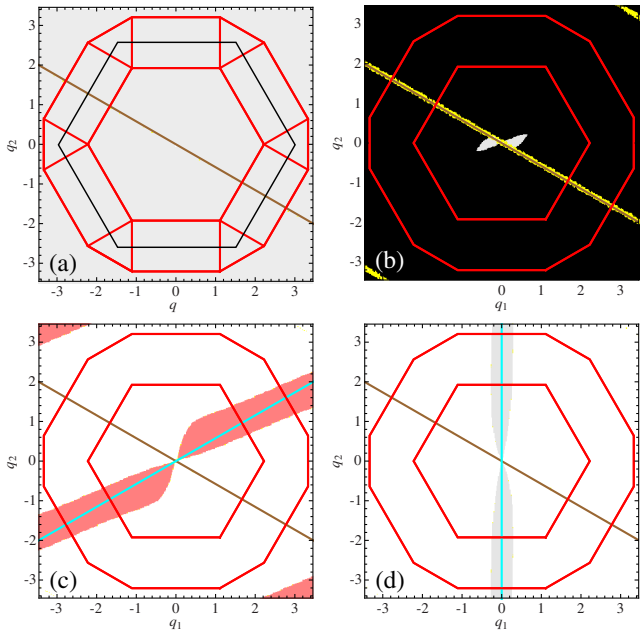

FIG. 2. Winding numbers m_1, m_2, and m_3 for (a) X_1 and (b)–(d) X_{-1}. q_1 and q_2 are the components of the respective $\mathbf{q}_\perp$ s. The (red) polygons depict projections of the edges of the top and equatorial surfaces of the BZ onto these planes. The black polygon in (a) represents the surface BZ. The color-coding of the shaded areas is as follows: pink corresponds to winding number 1, white to 0, gray to -1, and black to -2. Yellow indicates points where the numerical integration failed to converge properly. The (brown) solid lines indicate the twofold degenerate zero mode along the (1,1,1) direction. The (cyan) light line indicates the $(1, 1, -1)$ direction (guide to the eye).

where $\mathbf{q}_\perp$ specifies the components of $\mathbf{q}$ in the surface BZ of the lattice plane defined by $\mathbf{G}$, p is the component of $\mathbf{q}$ along $\mathbf{G}$, and $G = |\mathbf{G}|$. In practice, we calculate these winding numbers numerically using *Mathematica*. In fully gapped systems, the winding numbers are independent of $\mathbf{q}_\perp$. In systems with Weyl singularities, they are not. We use this fact to detect and map out Weyl singularities in the GPL. The idea is to calculate the winding numbers for an entire set of $\mathbf{q}_\perp$'s in a given surface BZ. For example, for our integration along $\mathbf{b}_1$, we sweep the BZ that is spanned by the unit vectors $\hat{\mathbf{c}}_{1,1} = (\mathbf{b}_1 \times \mathbf{b}_2)/|\mathbf{b}_1 \times \mathbf{b}_2|$ and $\hat{\mathbf{c}}_{1,2} = (\mathbf{b}_1 \times \hat{\mathbf{c}}_{1,1})/|\mathbf{b}_1 \times \hat{\mathbf{c}}_{1,1}|$. Figure 2 compiles our results for the winding numbers $m_i(\mathbf{q}_\perp) \equiv m(\mathbf{q}_\perp, \mathbf{G} = \mathbf{b}_i)$.

There is a qualitative difference between X_{+1} and X_{-1} in the values and distribution of their winding numbers: For X_1, $m_i = -1$ throughout the surface BZ associated with each $\mathbf{b}_i$. For X_{-1}, boundaries determined by the projections of WLs onto any given surface BZ divide the latter into regions with different winding numbers. In addition to the WLs, for both X_1 and X_{-1} there is a twofold degenerate line of ZMs along the (1,1,1) direction (that we verify by diagonalizing $\mathbf{D}$ for $\mathbf{q}$ along $\hat{\mathbf{n}}$) whose winding number is zero. This line is a consequence of the $\mathbf{q}_\perp = 0$ SSS of the flat GKL planes in the GPL. In the more general version of our GPL, alluded to above, this line splits up into two oppositely charged WLs when the reference positions of one of the basis sites 1, 2, or 3 is moved out of the GKL plane. These WLs are separated by a distance proportional to the distance of the respective sites from the GKL plane.

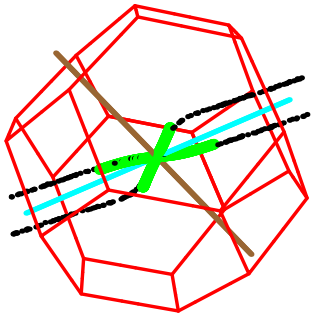

FIG. 3. WLs for X_{-1} traversing the (red) dedocahedron-shaped BZ. The (black) points mark our numerical reconstruction of the WLs, the (green) lines them stem from our analytical estimate. For X_1, only the twofold degenerate (brown) line along the (1,1,1) direction is present.

We can reconstruct the WLs in 3D from their projections onto the 2D BZs defined by the $\mathbf{b}_i$'s shown in Fig 2: A point on a projected line with coordinates (q_1, q_2) in the plane perpendicular to $\mathbf{b}_1$ is replaced by $\mathbf{q} = p\hat{\mathbf{b}}_1 + q_1\hat{\mathbf{c}}_{1,1} + q_2\hat{\mathbf{c}}_{1,2}$, where $\hat{\mathbf{b}}_1 = \mathbf{b}_1/|\mathbf{b}_1|$, and likewise for the projection onto the plane perpendicular to $\mathbf{b}_2$. Then, we calculate the intersections of the resulting manifolds. Finally, we discard all intersection points whose projections onto the plane perpendicular to $\mathbf{b}_3$ are incompatible with our results for m_3. Our results for the WLs in 3D are depicted in Fig. 3. As follows from the previous paragraph, the only ZMs that we encounter for X_1 lie on a line along $\hat{\mathbf{n}}$. For X_{-1} there is in addition a pair of WLs. These WLs do not form closed loops but follow a path in the BZ between points separated by a RL vector.

It is informative to compare our numerical results to analytical predictions for the WLs. To this end, we consider small deviations about the PL as parametrized by $X_\varepsilon \equiv (\varepsilon, \varepsilon, \varepsilon, \varepsilon)$ and $X_{-\varepsilon} \equiv (-\varepsilon, \varepsilon, \varepsilon, \varepsilon)$, and we expand $\det \mathbf{C}(\mathbf{q})$ in powers of the q_i and ε. For both X_ε and $X_{-\varepsilon}$, the resulting expansion is of the form

$$\det \mathbf{C} = f^{(3)}(\mathbf{q})\varepsilon^3 + f^{(4)}(\mathbf{q})\varepsilon^2 + f^{(5)}(\mathbf{q})\varepsilon + O(q_i^6), \qquad (3)$$

where the $f^{(m)}(\mathbf{q})$ are different functions of mth order in q_i for X_ε and $X_{-\varepsilon}$ that vanish for any $\mathbf{q}$ along $\hat{\mathbf{n}}$. We solve for the wave vectors that are zeros of the right-hand side of Eq. (3). For X_ε, there is only one real solution that corresponds to any $\mathbf{q}$ along $\hat{\mathbf{n}}$. For $X_{-\varepsilon}$, there are additional real solutions, which we display for $\varepsilon = 0.1$ in Fig. 3. Note the nice agreement at small q between the numerical and analytical results for X_1 and X_{-1}.

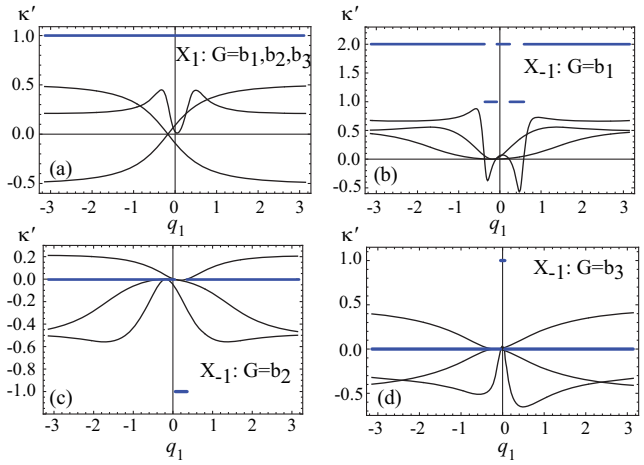

FIG. 4. κ' (black lines) and ν_T (blue straight lines) of surface ZMs with fixed $q_2 = 0.1$ for (a) X_1 and (b)–(d) X_{-1}.

Now, we turn to surface modes. In general, the total edge index $\nu(\mathbf{q}_\perp, \mathbf{G}) = n_0(\mathbf{q}_\perp, \mathbf{G}) - s(\mathbf{q}_\perp, \mathbf{G})$ is the sum of a local part $\nu_L(\mathbf{G})$ [1,3], which is independent of $\mathbf{q}_\perp$, and a topological part $\nu_T(\mathbf{q}_\perp, \mathbf{G})$. At free surfaces, $s(\mathbf{q}_\perp, \mathbf{G}) = 0$, and $\nu(\mathbf{q}_\perp, \mathbf{G}) = n_0(\mathbf{q}_\perp, \mathbf{G})$. The local count is $\mathbf{G} \cdot \mathbf{R}_L/(2\pi)$, where $\mathbf{G}$ is the *outer* normal to its lattice plane and $\mathbf{R}_L$ is the difference between the dipole moment of the surface unit cell and that of the reference cell of Fig. 1 (see Supplemental Material [23]). In systems without Weyl singularities, the winding numbers m_i are independent of wave vector as mentioned above and define a topological charge $\mathbf{R}_T = \sum_i m_i \mathbf{T}_i$. For X_1, in particular, $\mathbf{R}_T = -(2, 2, 2)$. The topological surface count in these systems is simply $\nu_T(\mathbf{G}) = \mathbf{G} \cdot \mathbf{R}_T/(2\pi)$, independent of $\mathbf{q}_\perp$. In systems with Weyl singularities, the topological count $\nu_T(\mathbf{q}_\perp, \mathbf{G}) = m(\mathbf{q}_\perp, \mathbf{G})$ depends on $\mathbf{q}_\perp$ and is not defined globally.

For simplicity, we focus here on surfaces whose normals are parallel to primitive vectors $\mathbf{b}_i$ of the RL. We calculate the complex inverse penetration depths $\kappa(\mathbf{q}_\perp)$ by setting $\mathbf{q} = i\kappa\mathbf{b}_1 + q_1\hat{\mathbf{c}}_{1,1} + q_2\hat{\mathbf{c}}_{1,2}$, and similarly for $i = 2, 3$, and solving for the roots of $\det \mathbf{C}(i\kappa, q_1, q_2) = 0$. Positive (negative) values of $\kappa' \equiv \mathrm{Re}(\kappa)$ correspond to ZMs that decay in the direction of $\mathbf{b}_1$ ($-\mathbf{b}_1$) and that are, therefore, localized on the surface with outer normal along $-\mathbf{b}_1$ ($\mathbf{b}_1$). Figure 4 presents plots of κ' and $\nu_{T,i} = \nu_T(-\mathbf{b}_i)$ as a function of q_1 and fixed $q_2 = 0.1$ for our three surface orientations and for X_1 and X_{-1}. For each X and $\mathbf{b}_i$, there are positive and negative values of κ' indicating localization on both surfaces, but as required by the Calladine-Maxwell theorem, there is always a total of three ZMs on the two surfaces. For X_1, the three κ's are the same function of q_1 for all $\mathbf{b}_i$s. In addition $\nu_{T,i} = 1$ is independent of i. This implies that $\nu_{L,i} = \nu_L(-\mathbf{b}_i) = 1$ for every i. ν_L is a property of a surface that does not change if the topological class is varied by changing X. For X_{-1}, the functions $\kappa'(q_1)$ are different for the different surfaces, and the number of positive and negative values undergo discontinuous changes in accord with similar changes in $\nu_{T,i}(q_1)$. At the $-\mathbf{b}_1$ surface, ν_{T1} takes on values of 2 and 1, and, as required, the number of modes localized on the $-\mathbf{b}_1$ surface changes from 2 to 1 and back again with the jumps in ν_{T1}. Similarly, for the $-\mathbf{b}_2$ surface, $\nu_{T,2}$ takes on values 0 and -1 and $n_0(q_1, -\mathbf{b}_2)$ values 1 and 0 (though the latter region is relatively small), and for the $-\mathbf{b}_3$ surface, ν_{T3} is zero almost everywhere except for a very small region near the origin where it is equal to 1 and $\nu_3(q_1, -\mathbf{b}_3)$ is either 1 or 0. In the Supplemental Material [23], we provide more detail about the calculation of $\mathbf{R}_L$, and we show results for surfaces perpendicular to the $\mathbf{G} = \pm 2\pi(1, 0, 0)$ RL vector. In this case, four bonds must be cut to liberate a strip, and there are four surface ZMs distributed between the two surfaces.

In conclusion, we have studied topological phonons in 3D in a generalized pyrochlore lattice. Our model lattice displays distinct topological states and thereby underscores the validity in 3D of the general theory for topological phonons laid out in Ref. [3]. Together with the recent work on generalized square lattices [16] and 2D models of jammed matter [17], our work hints that Weyl singularities are a common feature in Maxwell lattices and that the GKL is special in that its unit cell does not provide enough degrees of freedom to have them. The present work indicates that the GPL is a candidate for detecting Weyl lines in mechanical experiments on GPL-like metamaterials which should become producible by 3D-printing technologies in the foreseeable future.

This work was supported by the NSF under No. DMR-1104701 (O. S., T. C. L.) and No. DMR-1120901 (O. S., T. C. L.). C. L. K was supported by a Simons Investigators Grant and T. C. L. by a Simons Fellows grant.

[1] T. C. Lubensky, C. L. Kane, X. Mao, A. Souslov, and K. Sun, Rep. Prog. Phys. **78**, 073901 (2015).
[2] K. Sun, A. Souslov, X. Mao, and T. C. Lubensky, Proc. Natl. Acad. Sci. U.S.A. **109**, 12369 (2012).
[3] C. Kane and T. C. Lubensky, Nat. Phys. **10**, 39 (2014).
[4] W. P. Su, J. R. Schrieffer, and A. J. Heeger, Phys. Rev. Lett. **42**, 1698 (1979).
[5] B. I. Halperin, Phys. Rev. B **25**, 2185 (1982).
[6] F. D. M. Haldane, Phys. Rev. Lett. **61**, 2015 (1988).
[7] C. L. Kane and E. J. Mele, Phys. Rev. Lett. **95**, 146802 (2005).
[8] B. A. Bernevig, T. L. Hughes, and S.-C. Zhang, Science **314**, 1757 (2006).
[9] J. E. Moore and L. Balents, Phys. Rev. B **75**, 121306 (2007).
[10] L. Fu, C. L. Kane, and E. J. Mele, Phys. Rev. Lett. **98**, 106803 (2007).
[11] Z. Hasan and C. Kane, Rev. Mod. Phys. **82**, 3045 (2010).
[12] X.-L. Qi and S.-C. Zhang, Rev. Mod. Phys. **83**, 1057 (2011).
[13] B. G. Chen, N. Upadhyaya, and V. Vitelli, Proc. Natl. Acad. Sci. U.S.A. **111**, 13004 (2014).

[14] J. Paulose, B. G. Chen, and V. Vitelli, Nat. Phys. **11**, 153 (2015).
[15] J. Paulose, A. S. Meeussen, and V. Vitelli, Proc. Natl. Acad. Sci. U.S.A. **112**, 7639 (2015).
[16] D. Zeb Rocklin, B. Gin-ge Chen, M. Falk, V. Vitelli, and T. C. Lubensky, Phys. Rev. Lett. **116**, 135503 (2016).
[17] D. Sussman, O. Stenull, and T. C. Lubensky, Soft Matter **12**, 6079 (2016).
[18] G. Volovik, Lect. Notes Phys. **718**, 31 (2007).
[19] A. A. Burkov, M. D. Hook, and L. Balents, Phys. Rev. B **84**, 235126 (2011).
[20] Y. Kim, B. J. Wieder, C. L. Kane, and A. M. Rappe, Phys. Rev. Lett. **115**, 036806 (2015).
[21] R. Yu, H. M. Weng, Z. Fang, X. Dai, and X. Hu, Phys. Rev. Lett. **115**, 036807 (2015).
[22] L. Lu, L. Fu, J. D. Joannopoulos, and M. Soljacic, Nat. Photonics **7**, 294 (2013).
[23] See Supplemental Material at http://link.aps.org/supplemental/10.1103/PhysRevLett.117.068001 for a brief review of the GKL, details of the equilibrium matrix and the calculation of surface zero modes.
[24] J. C. Maxwell, Philos. Mag. **27**, 294 (1864).
[25] C. R. Calladine, Int. J. Solids Struct. **14**, 161 (1978).
[26] X. G. Wan, A. M. Turner, A. Vishwanath, and S. Y. Savrasov, Phys. Rev. B **83**, 205101 (2011).
[27] S.-Y. Xu, I. Belopolski, A. Nasser, M. Neupane, G. Bian, C. Zhang, R. Sankar, G. Chang, Z. Yuan, C.-C. Lee, S.-M. Huang, H. Zheng, J. Ma, D. S. Sanchez, B. Wang, A. Bansil, F. Chou, P. P. Shibayev, H. Lin, S. Jia, and M. Z. Hasan, Science **349**, 613 (2015).
[28] D. P. DiVincenzo and E. J. Mele, Phys. Rev. B **29**, 1685 (1984).
[29] A. H. Castro Neto, F. Guinea, N. M. R. Peres, K. S. Novoselov, and A. K. Geim, Rev. Mod. Phys. **81**, 109 (2009).
[30] S. M. Young and C. L. Kane, Phys. Rev. Lett. **115**, 126803 (2015).
[31] C. Kittel, *Introduction to Solid State Physics*, 4th ed. (John Wiley and Sons, New York, 1971).
[32] S. D. Guest and J. W. Hutchinson, J. Mech. Phys. Solids **51**, 383 (2003).